Myolink: A 128-Channel, 18 nV/$\sqrt{\text{Hz}}$, Embedded Recording System, Optimized for High-Density Surface Electromyogram Acquisition

Simos Koutsoftidis, *Student Member, IEEE*, Deren Y. Barsakcioglu, *Member, IEEE*, Konstantinos Petkos, *Member, IEEE*, Dario Farina, *Fellow, IEEE*, and E. M. Drakakis, *Member, IEEE*

Abstract*—*Objective: **We present Myolink, a portable, modular, low-noise electrophysiology amplifier optimized for high-density surface electromyogram (HD sEMG) acquisition.** ***Methods:*** **Myolink consists of 4 modules. Each 10 $\times$ 8 cm module can concurrently acquire 32 unipolar electrode potentials at sampling rates of up to 8 kHz with 24-bit resolution. Modules may be stacked and operated synchronously, supporting the concurrent acquisition of up to 128 channels. A custom high-performance analog front-end provides an input-referred-noise $< 0.4\ \mu\text{V}_{\text{RMS}}$ for a bandwidth of 23–524 Hz (tuneable by design choices), which is lower than current commercial systems. Digitized signals are processed by a custom on-board FPGA-based controller and subsequently transmitted to a PC via a medical-grade isolated USB 2.0 interface.** ***Results:*** **The system has been tested by recording experimental HD sEMG signals, which have been subsequently decomposed into motor unit action potentials. Compared to commercially available systems, the proposed recording system led to higher-quality surface EMG acquisition, as well as higher decomposition accuracy across a wide range of forces, with the greater gain for forces $\leq$ 20% of the maximum voluntary contraction.** ***Significance:*** **A portable, ultra-low-noise, HD sEMG amplifier design has been implemented and characterized. The system provides IRN performance beyond the capabilities of current state-of-the-art instrumentation and this improvement has a significant effect on HD sEMG decomposition.**

***Index Terms*—Electromyography, high-density, low noise, multi-channel, neural interfacing, recording.**

I. Introduction

HIGH density surface Electromyography (HD sEMG) has been an invaluable tool in neuromuscular research and clinical applications for the last two decades. Among its uses, HD sEMG is applied for prosthetic control as well as fundamental physiological and kinesiological investigations [1]. Recently, by exploiting advanced signal processing and blind source separation algorithms [2], [3], HD sEMG decomposition has provided the means to decode individual motor unit activation patterns non-invasively [4]. This decoding can be used for non-invasive human-machine interfacing [5], and has recently been applied in a series of studies on real-time biofeedback and control [6], [7].

The quality of the information extracted from HD sEMG signals is ultimately influenced by the signal-to-noise ratio (SNR) of the recording, which influences the subsequent signal processing stages [8]. Noise in EMG recordings results from the amplifier input-referred-noise (IRN), the electrode-skin interface noise, stability in electrode-skin impedance and electromagnetic/mains interference (EMI) [9]. Previous work has shown that under well controlled recording setups, the noise contribution of the electrode-skin interface and EMI can be reduced to levels comparable with the IRN of EMG amplifiers, within the typical EMG bandwidth [10], [11]. Specifically, electrode-skin interface noise is mostly prevalent below 10 Hz.

HD sEMG acquisition is mainly performed using specialized recording instrumentation due to the large number of low-noise channels and relatively small bandwidth required (typically $<$ 500 Hz). The typical IRN of existing multi-channel electrophysiology amplifiers within the EMG bandwidth ranges between 1–10 μV_{RMS}. Significant reductions in IRN have been recently made possible by advances in performance and miniaturization of state-of-the-art, off-the-shelf integrated circuits (ICs) [12], [13]. While these IRN improvements have been demonstrated for systems of up to 8 channels, benefits to HD sEMG remain unexplored due to the lack of appropriately scaled-up multi-channel instrumentation. Specifically, IRN performance must be achieved given stricter area per channel constrains if system size is limited within a portable footprint to facilitate wearability. Wearability is often desirable in HD sEMG applications as it provides greater freedom of movement to the patient, enabling experimentation outside the confines of traditional laboratory settings.

Whilst portable and even wireless HD sEMG recording systems have been developed [14], [15], they compromise performance (e.g. IRN, input impedance, common-mode rejection

Manuscript received 2 August 2021; revised 16 January 2022 and 31 March 2022; accepted 16 April 2022. Date of publication 25 April 2022; date of current version 20 October 2022. This work was supported in part by the Imperial College Confidence in Concept under Grant P81130, in part by the ERC Synergy Project NaturalBionicS under Grant 810346, and in part by the EPSRC Transformative Healthcare NISNEM Technology under Grant EP/T020970/1. *(Simos Koutsoftidis and Deren Y. Barsakcioglu are co-first authors.) (Dario Farina and E. M. Drakakis are co-senior authors.) (Corresponding authors: Dario Farina; E. M. Drakakis.)*

Simos Koutsoftidis, Deren Y. Barsakcioglu, and Konstantinos Petkos are with the Department of Bioengineering, Imperial College London, U.K.

Dario Farina and E. M. Drakakis are with the Department of Bioengineering, Imperial College London, SW7 2AZ London, U.K (e-mail: d.farina@imperial.ac.uk; e.drakakis@imperial.ac.uk).

Digital Object Identifier 10.1109/TBME.2022.3170025

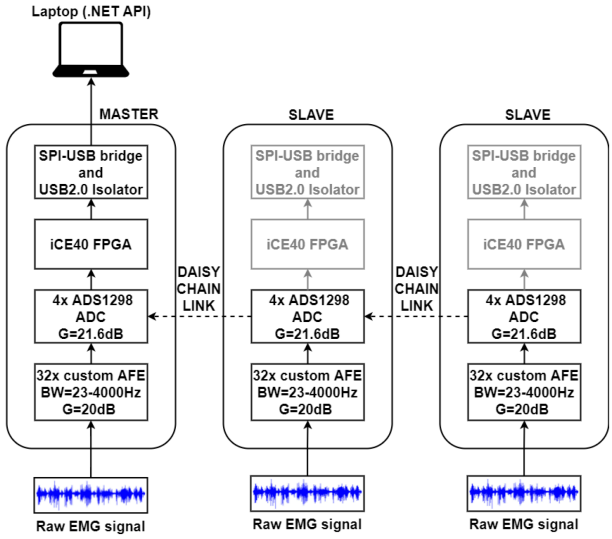

Fig. 1. System level design and proposed modularity scheme. Circuits contained in gray blocks are disabled during slave operation.

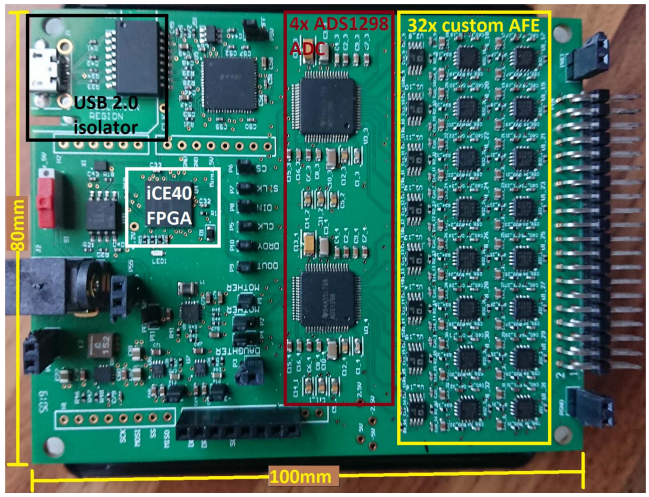

Fig. 2. Recording amplifier PCBA. The board stack is a standard 1.6 mm using six layers (4 signal, 2 power). Note that the AFE and ADC designs are also mirrored to the solder side of the board; totaling 32 recording channels.

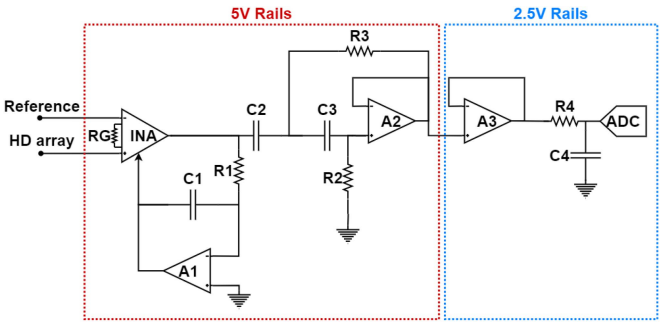

Fig. 3. The analog front-end topology utilized. All components required to implement the AFE are displayed, excluding power-supply decoupling capacitors. The component parameter values are detailed in Table I.

ratio) or overall channel count with respect to desktop-based systems. Here, we describe the development and test of a compact, HD sEMG recording system providing state-of-the-art electronic performance, portability as well as comparable channel count to that offered by larger desktop-based systems; with the latter accomplished through the employment of modularity. System design, experimental protocols and details of analysis are explained in Section II. This is followed by results of the experimental measurements and analysis in Section III. Section IV discusses the findings and future improvements. Conclusions are drawn in Section V.

II. Methods

A. Hardware Design Approach

As this work was primarily focused on achieving electronic performance beyond the capabilities of currently available dedicated single-chip solutions, we implemented a custom, compact, low-noise analog front-end (AFE) using discrete amplifier ICs. The system comprises modules featuring 32 AFEs each, which amplify and condition raw signals acquired from HD sEMG electrode arrays in unipolar configuration. Embedded, high-resolution, discrete analog-to-digital converters (ADCs) digitize these conditioned signals. A low-power Field Programmable Gate Array (FPGA) based system controller configures the ADC modules and interfaces the raw data with an SPI to USB bridge circuit. Raw data are accessible by a Windows PC through an isolated USB 2.0 interface. High-efficiency DC/DC converters have been utilized to maintain the module power consumption under 2 W, supporting short-term battery-powered operation. The system level design is summarized in Fig. 1.

Up to four 32-channel amplifier modules can be stacked and operated synchronously to increase the channel count, using a single FPGA controller. This is achieved by two hardware configurable modes of system operation; a "master" and a "slave" mode. In master mode, all aforementioned circuit blocks are active, whereas in slave mode only the front-ends, ADCs and power supply are operated. Data is transmitted between boards through an ADC daisy-chain link, from the last slave board to the single master board, as illustrated in Fig. 1. This approach supports simultaneous acquisition of up to 128 channels at a typical 2 kHz sampling rate and 24-bit resolution. Fabrication cost is minimized as only a single printed-circuit-board-assembly (PCBA) design needs to be realized. Furthermore, when modules are to be operated solely in slave configuration, the digital back-ends may be left unpopulated during the board assembly process to further reduce the cost. A complete 32-channel amplifier module is shown in Fig. 2.

B. Analog Front-End

The AFE design, illustrated in Fig. 3, consists of a low-noise Instrumentation Amplifier (INA) first-stage, which exhibits a high (> 110 dB) common-mode-rejection-ratio (CMRR) to attenuate mains interference, and very high input impedance ($> 100\ G\Omega \parallel 2$ pF) to prevent loading from high-impedance electrodes. Active AC-coupling through a DC servo amplifier driving the INA reference pin was preferred over more traditional R-C passive implementations in order to eliminate the thermal noise and impedance mismatch errors associated with input resistors. The INA gain was set at 20 dB and ± 5 V front-end

TABLE I
AFE COMPONENTS UTILIZED (SEE FIG. 3)

Designator	Component	Value	Tolerance
C1	X7R Capacitor	680nF	10%
C2,C3	X7R Capacitor	1.5μF	10%
C4	X7R Capacitor	100nF	10%
R1	AD8295 IC resistor	20KΩ	0.1%
R2	Film Resistor	7.87KΩ	0.1%
R3	Film Resistor	4.02KΩ	0.1%
R4	Film Resistor	400Ω	0.1%
RG	Film Resistor	5.49KΩ	0.1%
INA	AD8295	-	-
A1	AD8295	-	-
A2	AD8295	-	-
A3	ADA4177	-	-

rails were utilized to provide ±600 mV DC offset tolerance thus preventing amplifier clipping due to input offsets generated by the electrode-skin interface, as described in [16]. A 2^{nd} order Sallen-Key Butterworth high-pass filter with its cut-off frequency set at 20 Hz has been implemented in order to attenuate any residual DC offsets and motion artifacts, as recommended in [17]. When combined with the active AC-coupling circuit, the designed filter forms a 3^{rd} order Bessel high-pass filter with a cut-off frequency of 23 Hz. This exhibits higher roll-off and comparable transient response to the 2^{nd} order filter. It has to be noted that the choice of this cut-off frequency is a compromise for a wide range of applications but does not correspond to the optimal cut-off frequency for specific applications. For example, for physiological investigations, a high-pass cut-off frequency not greater than 10 Hz is often suggested [18]. Optimised high-pass cut-off frequencies for specific applications can be implemented by changing the values of resistors R1-R3 in the filter. The filter design in this paper does not preclude greater bandwidths by small changes in the filter components.

Additional 21.6 dB of analog gain is applied by the integrated programmable gain amplifiers (PGA) of the ADC to reduce the IRN contribution of the converters and to increase the effective resolution. The INA, DC servo and Sallen-Key amplifiers (operational Amplifiers A1 and A2 in Fig. 3) have been realized using a single integrated circuit (AD8295, Analog Devices, Norwood, MA) to minimize the board area. A 1^{st} order low-pass filter with cut-off at 4 kHz has been implemented for anti-aliasing purposes, providing over 40 dB attenuation to any interference falling on the harmonics of the converter's $\Delta\Sigma$ modulator. It is driven by a low-noise, buffer amplifier (operational amplifier A3 in Fig. 3) with integrated input overvoltage protection (ADA4177, Analog Devices, Norwood, MA), supplied by the same ±2.5 V rail as the ADC. The addition of this buffer stage protects the converter against input signals exceeding ±2.5 V, which may be generated by the output of A2 on the ±5 V side. Low-pass band-limiting has been intentionally left to the integrated 3^{rd} order digital sinc filters of the $\Delta\Sigma$ ADC, set at $0.262 \times Fsampling$ and enabling bandwidth tuneability.

C. ADC and Digital Back-End

Four 8-channel, low-noise, 24-bit, ADC ICs with integrated programmable gain amplifiers (ADS1298, Texas Instruments, Dallas, TX) have been utilized to provide sufficient quantization resolution to match the IRN performance of the AFEs (25 nV/bit when the PGA's gain is set at 21.6 dB). All four ICs share the same master clock and SPI configuration lines in order to ensure synchronous operation. Sampling frequencies of 1, 2, 4, 8 kHz with corresponding signal bandwidths of 256, 524, 1048, 2096 Hz are feasible for each 32-channel module. Raw ADC data are collected through a proprietary daisy-chain interface. This chain may be expanded to accommodate up to 16 ADCs, from four 32-channel systems, using the board configuration scheme discussed in Section II-A. Data from all ADCs are acquired and processed by an on-board FPGA-based controller (ICE40-HX8K Lattice Semi-conductor, Portland, OR) and subsequently transmitted to an SPI-USB bridge circuit (FT2232H, Future Technology Devices International, Glasgow, U.K.) for interfacing with the PC. The USB data lines are isolated using an IEC-60601-1 compliant digital isolator IC (ADuM4160, Analog Devices, Norwood, MA) which, when combined with battery-powered operation or with a medically approved AC/DC supply, ensure electronic compliance with basic patient isolation requirements.

D. Power Supply

The power supply section generates the ±2.5 V, ±5 V analog rails, a 3.3 V rail for all digital circuitry as well as a 1.2 V rail for the FPGA controller core. A high-efficiency, buck-boost DC/DC converter (TPS60301, Texas Instruments, Dallas, TX) powers all regulators from the DC input and delivers the +5 V rail, supporting a wide (2-16 V) supply range for battery-powered operation. Two low-noise voltage inverters (LM27761, Texas Instruments, Dallas, TX) are utilized to provide the −2.5 V and −5 V analog rails. A power management IC (TPS65000, Texas Instruments, Dallas, TX) provides the 3.3 V rail, from the internal DC/DC converter, and the 2.5 V and 1.2 V rails from the two integrated low-dropout regulators.

E. Software Interface

A .NET-based Application Programming Interface (API), developed in C#, provides low-level access to the raw ADC data. The inherit block transfer nature of USB and interrupt driven operation of Windows necessitate packeting of several samples into blocks to optimise data transfer throughput and prevent data loss. This buffering is performed in the USB bridge IC. Data is requested by the API in blocks of 64, 128 and 256 samples for sampling frequencies of 2, 4 and 8 kHz respectively, maintaining a communication latency below 35 ms. A GUI has been developed on the Microsoft WinForms environment to enable data collection. Additionally, the API may be ported to Matlab or any other third-party software with basic support for .NET dynamic link libraries.

F. Electrical Characterization

The IRN was measured by shorting both working and reference INA inputs to system ground and recording the ADC output at 2 kHz for 10 seconds. The impulse response of the system was measured by applying a 20 mV peak square monophasic pulse of 2 ms duration across the AFE inputs. The DC level of the pulse

was varied from 0 V to 500 mV to evaluate the effect of input offsets. The step response of the system was measured by applying a step signal of variable amplitude across the AFE inputs. A 20 mV peak amplitude was used to demonstrate the response to steps within the maximum AC operating range whilst 300 mV and 500 mV steps were applied to record the response to steps within the DC operating range. The total-harmonic-distortion (THD) was evaluated by applying 80 Hz sinusoidal signals with peak amplitude ranging from 1 μV to 10 mV and recording the AFE output at 2 kHz for 120 seconds. THD was computed from the acquired signals based on their first five harmonics.

G. EMG Measurements and Experimental Validation

HD sEMG were recorded using 64-electrode gelled adhesive grids (GR08MM1305,OT Bioelettronica) mounted over the belly of the tibialis anterior muscle of five healthy participants (age: 28.2 $\pm$ 3.2 years, 2 females, 3 males). Prior to the placement of the HD sEMG grid, the skin was shaved and cleansed with abrasive paste and ethanol. Two moist strap electrodes were attached to the ankle area, one acting as the unipolar reference point, and the other as the system ground, providing a biasing path for the amplifiers through the participants. An ankle dynamometer (NEG1, OT Bioelettronica) was used to fix the foot of the participants (ankle flexed at 0°), allowing for the dorsiflexion of the foot. A force amplifier (Forza, OT Bioelettronica) was used together with the ankle dynamometer.

The recordings were performed using both Myolink and, for comparison, a state-of-the-art commercial multi-channel electrophysiology recording system (Quattrocento, OT Bioelettronica). The participants were asked to start the experiments by performing a maximum voluntary contraction (MVC) force in dorsiflexion. They were then presented with seven targets to follow. Each target consisted of a 5 s ramp up, 20 s of sustained contraction at a constant force level, and a 5 s ramp down. The force levels for sustained contractions were set at 3, 5, 10, 15, 20, 30 and 70 % of the MVC for each target. Between each contraction, a 30 s rest period was included to prevent muscle fatigue (except for 70% for which 2 min rest was provided prior to contraction). A custom graphical user interface (implemented in Matlab R2017b) was used to provide the participants with visual feedback on force as well as target trajectories to follow with the force feedback.

The data from both recording systems were digitally filtered by a 4^{th} order Butterworth 20–500 Hz band-pass filter, in order to compare the performance of the two systems over the same bandwidth. A 2^{nd} order notch filter with 2 Hz bandwidth and center frequency set at 50 Hz was applied to all acquired signals to eliminate the effect of residual mains interference in both cases. The recorded signals from both systems were then analyzed and compared in terms of EMG decomposition performance. EMG decomposition, in brief, consists in decoding the discharge patterns of the spinal motor neurons innervating the muscle from which the EMG signal is recorded. The surface EMG decomposition performance from both recording systems was analyzed offline. The total number of unique motor units (MUs) detected as well as the number of unique MUs decomposed at each contraction level were assessed. The separation vectors, which extracts the spiking activity of each motor unit, were determined for each contraction level (i.e. 3–70 % of the MVC) separately [2]. For decomposition, the number of iterations and the silhouette measure (SIL) threshold were set to 250 and 0.9, respectively.

Since the separation vectors were identified separately for each contraction level, it was likely that some MUs were identified at many contraction levels, hence some separation vectors could be duplicated. Therefore, these separation vectors were used to re-decompose the HD sEMG signals across all contraction levels and the discharges of each MU (across all contraction levels) were compared using the rate-of-agreement (RoA) metric [2]. If the RoA between the discharges of two identified MUs (across all contraction levels) was above 30%, these were considered as belonging to the same MU. The quality of the decomposition was also validated by computing the pulse-to-noise ratio (PNR) [19] and SIL [2] for each decomposed MU discharge pattern. In addition, the coefficient of variation of the inter-spike interval (COV_{ISI}) as well as the discharge rates were computed for each identified motor unit to ensure they were within the expected physiological boundaries. Statistical differences were tested using one-way analysis of variance following the Anderson-Darlington test for normality. For the cases where normality failed, Kruskalwallis one-way analysis of variance was used.

III. Results

A. Electrical Characterization

Electrical characterization measurements were performed as detailed in Section II-F at a typical electronics laboratory. IRN measurements were performed in the electrophysiology lab with both devices being battery-powered to ensure realistic EMI conditions. The measured frequency response for 32 amplifier channels, in the typical sEMG configuration, is displayed in Fig. 4(a). Bandwidth tuneability through alteration of the sampling frequency is demonstrated in Fig. 4(b). The recorded IRN spectra of both the Myolink and that of the commercial system are displayed in Fig. 4(c). The amplifier THD against input signal amplitude is shown in Fig. 4(d). The distribution of measured integrated IRN and THD across 32 channels is illustrated in Fig. 6(a) and (b) respectively. The amplifier step response and impulse response at different input DC offsets are displayed in Fig. 5(a) and (b) respectively.

B. EMG Measurements and Experimental Validation

A representative monopolar signal recorded from the tibialis anterior muscle of one participant with the Myolink at the lowest contraction level is shown in Fig. 7. The recordings were acquired using HD sEMG grids (64-channels) across contraction levels ranging from 3 to 70 % of the maximum voluntary contraction force. For comparison, the same experimental procedure was used to acquire HD sEMG using the control commercial amplifier. The acquired HD sEMG signals were then decomposed to extract the discharge times of the spinal motoneurons underlying the EMG activity (for details of the method, see above Section II-G).

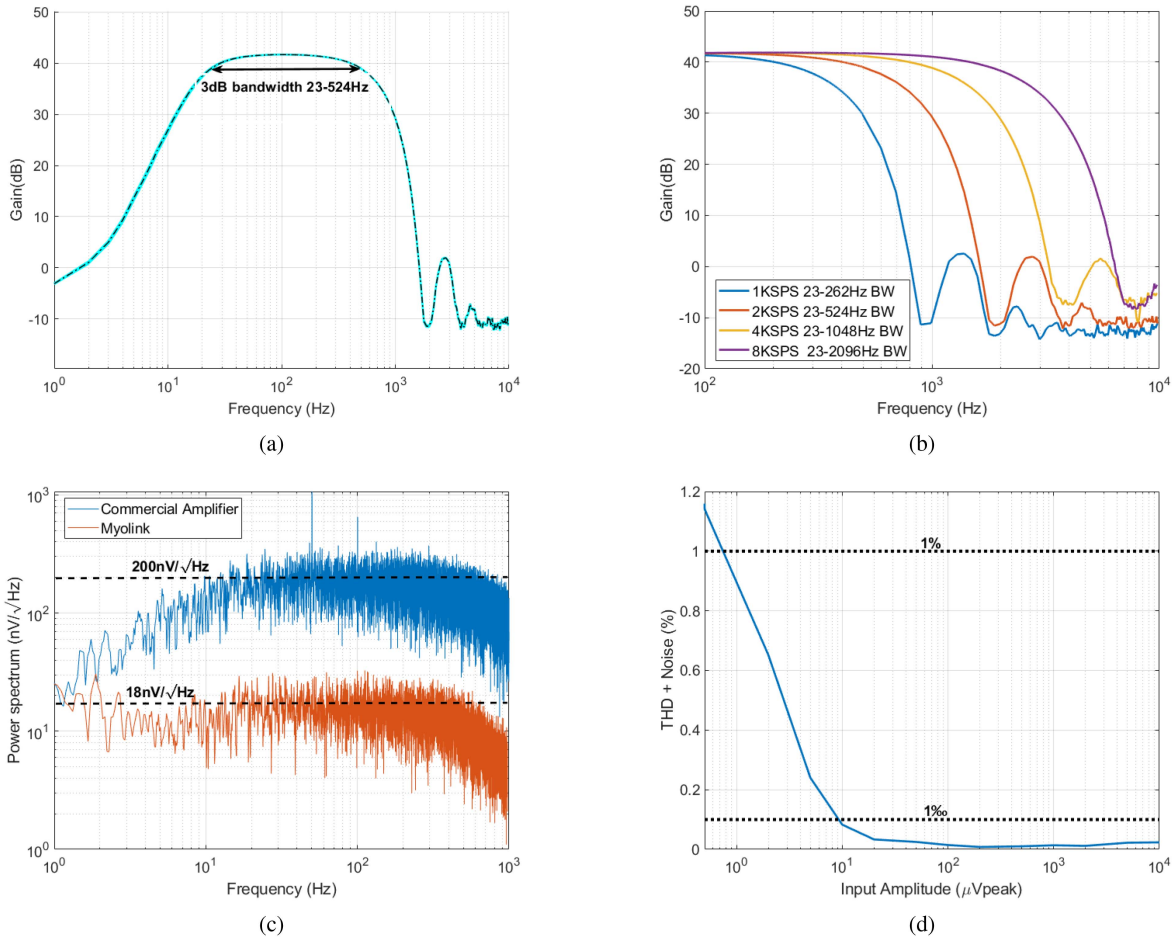

Fig. 4. Bode magnitude plots of the AFE response for the 32 channels. 2 kHz ADC sampling rate was used to limit the bandwidth to 524 Hz. The dotted line shows the mean channel response. The maximum Root Mean Square Error between the mean response and all other channel responses was below 0.02 dB (a). Bode magnitude plots of the AFE response for different sampling rates. Notch-like attenuation observed at multiples of the sampling frequency reflects the characteristic transfer function of sinc decimation filters, as entailed in the manufacturer's documentation (b). IRN spectrum of the proposed Myolink amplifier and a commercial system under identical ambient conditions without digital filtering applied. The integrated IRN spectrum value for a bandwidth of 23–524 Hz was 384 nV_{RMS} for Myolink and 3996 nV_{RMS} for the commercial system. Note that 50 Hz interference is also much less prominent for Myolink (c). THD as a function of the input signal peak amplitude. THD remains below 1% for signals between 1 μV and 10 mV. Furthermore, THD remains below 0.15% for signals between 10 μV and 10 mV, covering the typical EMG amplitude range (d).

The HD sEMG signals acquired with Myolink yielded a total number of 313 unique motor units (across all contraction levels and participants) with a median PNR of 40.8 dB (max - min: 54.8 dB and 30.1 dB) and a median SIL of 0.95 (max - min: 0.98 and 0.90). The median discharge rate and coefficient of variation of the interspike intervals were 9.8 pulses/sec and 23.6%. On the other hand, 249 unique motor units, with a median PNR of 38.8 dB (max - min: 65.1 dB and 30.1 dB) and median SIL of 0.93 (max - min: 0.97 and 0.90), were identified with the commercial amplifier. When the number of identified unique MUs was also analyzed for each contraction level, 18 unique MUs per force contraction level (median, max: 34, min: 3) were detected with the Myolink system. With the commercial system, on the other hand, 14 unique MUs per contraction level (median, max: 31, min: 3) were detected. In particular, the Myolink system outperformed the commercial system in identifying a higher number of unique MUs during force contraction levels $\leq 20\%$ of the MVC (Fig. 8).

This result should be attributed due to the ultra-low IRN performance of the Myolink system, which may allow the identification of smaller and/or deeper MUs than the commercial system [20]. To test this hypothesis, we further investigated the relative peak-to-peak amplitude of motor unit action potentials (MUAPs) detected by both systems. For each identified MU, the MUAP waveform detected in each channel was computed by averaging the EMG using the decomposed discharge times as triggers [21]. Each computed MUAP was 50 ms long (window centered at each action potential discharge time). For the analysis, only the MUAPs with absolute peak values above four times the baseline noise level were considered. The baseline noise levels were computed for each MUAP by computing the standard deviation of all samples during the first and last 15 ms of the MUAP window. For each contraction force level, the peak-to-peak amplitudes (V_{p-p}) of the detected MUAPs were then normalized with the median V_{p-p} obtained with the commercial system. This was done to allow comparison between V_{p-p}

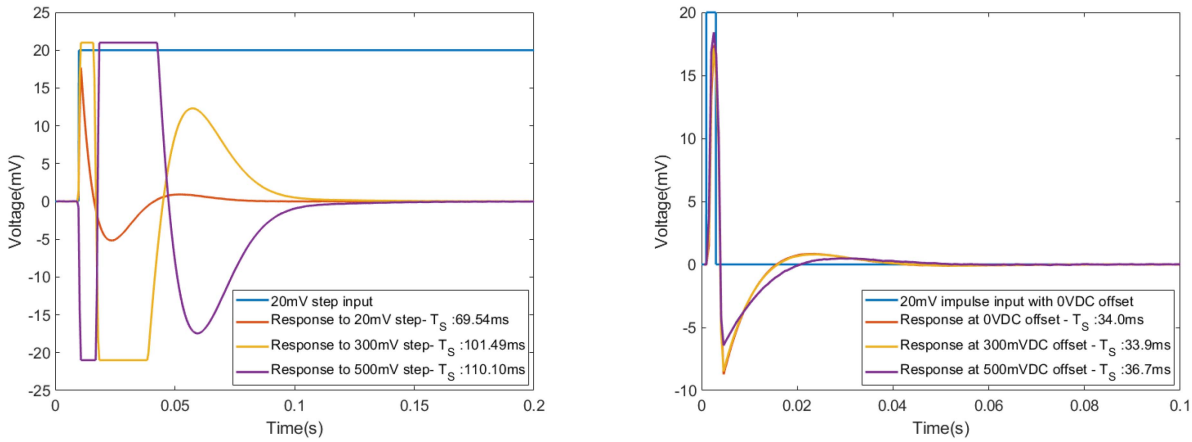

Fig. 5. AFE Step response to different amplitude steps (a). At 20 mV, the AFE settles according to the high-pass time constant. At 300 mV, the input AC range is briefly exceeded and amplifier clipping is observed. At 500 mV, the DC servo AC coupling stage saturates and high-pass filtering is only performed by the 2^{nd} order Butterworth second stage, causing a phase inversion in the stop-band. A 2% settling time of under 110 ms was observed in all cases. AFE Impulse response at different input DC levels (b). Note the slight increase of settling time at 500 mV offset relative to 300 mV. This is caused by the saturation of the AC-coupling circuit, effectively changing the AFE high-pass response from 3^{rd} order Bessel to 2^{nd} order Butterworth. A 2% settling time of under 40 ms was observed in all cases.

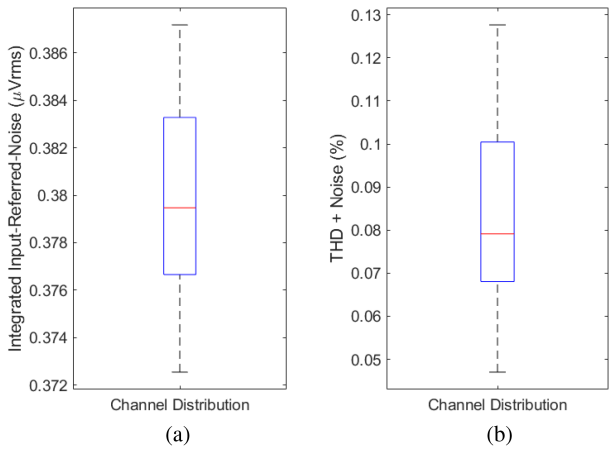

Fig. 6. Intra-channel distribution of integrated IRN across 32 AFEs (a). IRN was acquired across the bandwidth 23–524 Hz. Intra-channel distribution of THD across 32 AFEs (b). THD was acquired for an input signal of magnitude of 10 μVpeak and frequency of 80 Hz.

obtained at various contraction levels since absolute V_{p-p} will increase with the force contraction level. The results revealed comparable peak-to-peak MUAP amplitudes obtained by the Myolink and commercial amplifier with median peak-to-peak MUAP amplitudes obtained by the Myolink 5% higher than for the commercial amplifier.

IV. Discussion

We have developed a 128-channel portable embedded system for high-performance acquisition of HD sEMG signals. We have extensively validated the system through electrical characterization of its performance and experimental HD sEMG measurements. The recorded HD sEMG signals were further analyzed offline to assess the EMG decomposition performance for the potential use of Myolink in non-invasive neural interfacing applications.

TABLE II
Performance Comparison With Other EMG Recording Systems

Parameter	Units	This work	OTB Quattrocento	[15]	TMSI SAGA 32/64+	Biosemi Active-Two
Sampling frequency (FS)	KHz	1-8	0.5-10	2	4	2-16
Resolution	Bits	24	16	16	24	24
Maximum Bandwidth	Hz	23-0.26FS	0.7-4400	10-500	0-800	DC-0.2FS
Dynamic Range	mVp-p	42	33	10	300	524
DC offset tolerance	mV	600	-	400	150	262
R.M.S. IRN	μV	<0.4 (23-524Hz)	<4 (23-524Hz)	<3 (10-500Hz)	<0.8 (0.1-100Hz)	0.8 (0-400Hz)
Unipolar Channels	-	32-128	96-384	32	32-64	32-256
CMRR @50Hz	dB	>110	>95	82	>100	>90
Input Resistance	$G\Omega$	>100	>100	1.3	-	100
Area	cm^2	80	1070	7.5	251	285
Power per channel	mW	57.8	50.0	12.1	78.1	14.2

A comparison of the proposed system's electronic performance characteristics with typical commercial EMG amplifiers (Quattrocento, OT Bioelettronica, Turin, IT, Active-Two, BioSemi, Amsterdam, NL and SAGA32/64+, TMSI, Oldenzaal, NL) and an Intan-RHD2132-based wireless system is provided in Table II. Improvements are observed for IRN and CMRR relative to other systems, as a result of the first-stage INA and AFE architecture selected. Specifically, active AC-coupling combined with 20 dB front-end gain were utilized to achieve this performance with the AD8295 whilst also providing 600 mV tolerance to input DC offsets. At the time of writing, off-the-shelf discrete instrumentation amplifiers with superior performance

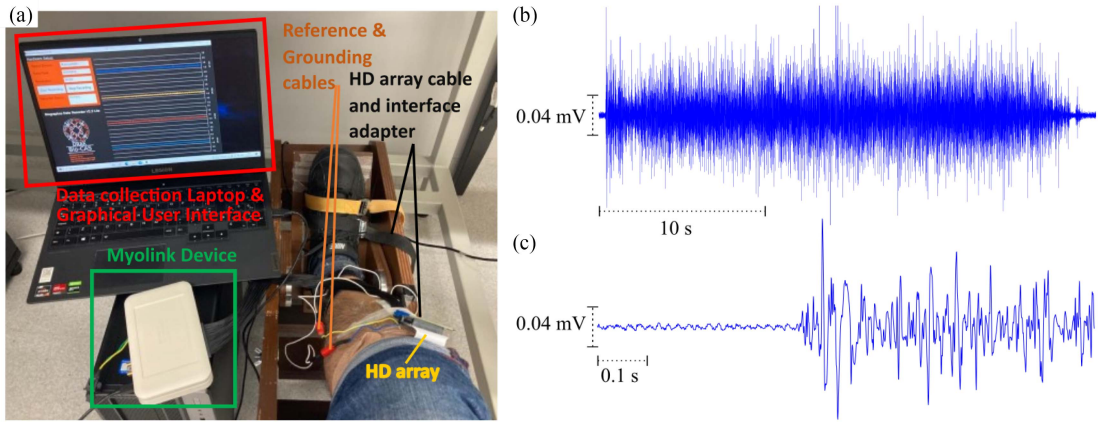

Fig. 7. Experimental setup and a representative EMG signal acquired with Myolink. (a) The Myolink, the Graphical User Interface, and the leg dynamometer. (b) A 30 s surface EMG signal acquired at 3% MVC force. (c) The initial 1 s of the signal presented in (b).

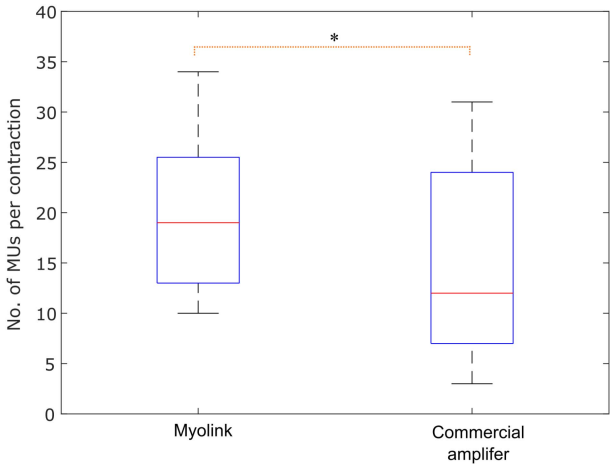

Fig. 8. The number of motor units (MUs) detected for each force contraction level are presented for force contraction levels equal to and less than 20% (i.e. 3%, 5%, 10%, 15% and 20% MVC). The HD sEMG signals were recorded with both Myolink and the commercial system used as a benchmark.

characteristics to the chip selected were also available on the market (AD84xx series, Analog Devices, Norwood, MA) but came in physically larger packages. The unique packaging of the AD8295 IC chosen enables implementation of all analog circuits within a very compact footprint (< 1.5 cm^2 per channel), significantly reducing board area. Performance comes at the expense of power consumption, with 57.8 mW required per channel. Employing typical low-profile, high-capacity (>8 Wh), Li-Ion batteries, which are widely used in portable devices, results in over 4 hours of operation for a 32 channel module. At the expense of raw analog performance, specialized single-chip mixed-signal AFE solutions, such as the ADS1299 (Texas Instruments, Dallas, TX) or RHD2132 (Intan Technologies, Los Angeles, CA) might be preferable to the proposed approach in applications where area and/or power consumption are deemed more critical. In either case, confining signal conditioning within the AFE, as in the work presented here, eliminates any computational requirements imposed by additional digital filtering, freeing up resources for more complex post-processing to be performed by the system controller.

An FPGA-based system controller was chosen over a dedicated microcontroller to provide maximum flexibility for future complex post-processing implementations. Wired data transmission via USB was selected over wireless protocols of comparable maximum baud rate to minimize communication latency, power consumption and ensure data integrity, which become critical when multiple devices are operated concurrently. Specifically, maximum sampling rate is limited to 2 kHz by the USB 2.0 Full-Speed data interface when 128-channels are acquired. This is acceptable for sEMG acquisition since signal power is below 500 Hz. In applications requiring higher sampling rates, USB 3.0 or Ethernet can be used to eliminate the data transmission bottleneck.

Following the characterization of the electronic performance, we have further tested the EMG decomposition performance from the recordings obtained by means of the Myolink. The main objective of the analysis was to ensure high-quality acquisition of surface EMG signals and to assess its feasibility in wearable non-invasive neural interfacing applications, leveraging upon its ultra-low noise performance and compact form factor. As a comparison benchmark, a state-of-the-art commercial amplifier - which has been used extensively in physiological investigations and proof-of-concept demonstration of emerging HD sEMG-based non-invasive neural interfaces - was used in the analysis. Both systems were tested under the same conditions and their EMG decomposition performance was compared in terms of the unique number of motor units identified and quality of the decomposition.

The results showed a similar decomposition quality for the two systems with no significant difference in PNR, SIL and CoV% values. On the other hand, the decomposition results with recordings from the Myolink system showed a significant increase in the number of uniquely identified MUs across all recordings. The advantage of the Myolink system was particularly evident for low contraction forces ($\leq 20\%$ MVC). We hypothesized that the greater number of identified MUs when using the Myolink may be due to detection of smaller energy

MUAPs (arising from smaller and/or deeper MUs) owing to Myolink's ultra-low noise performance. However, the comparison of action potential amplitudes for the MUs identified with the two systems did not confirm this hypothesis. The amplitude analysis was also repeated by modifying the MUAP exclusion criteria which was originally set to four times the baseline noise. The repeated analyses (including no exclusion condition) revealed similar results and no significant differences in MUAP amplitudes obtained by the two systems. Nevertheless, the results of the decomposition confirm the importance of ultra-low IRN to decomposition performance.

In our comparisons, we wanted to demonstrate the effect of IRN on decomposition performance and evaluate Myolink against widely-used commercially available systems for high-density EMG acquisition. Among the systems presented in Table I, we only had access to Quattrocento (OT Bioelettronica). While we expect the results to vary depending on the choice of commercial system compared, we still expect the relationship between IRN and decomposition performance to be valid.

V. Conclusion

A scalable, multi-channel, embedded recording system optimized for HD sEMG has been presented and tested. The device exhibits significantly lower IRN relative to existing, commercial systems whilst maintaining a portable PCBA footprint, primarily due to the custom high-performance AFE design. The corresponding increase in the SNR of the acquired EMG signals has been shown to improve MU decomposition performance proving its feasibility for portable high-quality non-invasive neural interfacing applications.

Acknowledgment

This study utilised the expertise and equipment at the Imperial College Advanced Hackspace.

References

[1] D. Farina *et al.*, "Principles of motor unit physiology evolve with advances in technology," *Physiology*, vol. 31, no. 2, pp. 83–94, 2016.

[2] F. Negro *et al.*, "Multi-channel intramuscular and surface EMG decomposition by convolutive blind source separation," *J. Neural Eng.*, vol. 13, no. 2, 2016, Art. no. 026027.

[3] A. Holobar and D. Zazula, "Multichannel blind source separation using convolution kernel compensation," *IEEE Trans. Signal Process.*, vol. 55, no. 9, pp. 4487–4496, Sep. 2007.

[4] D. Farina and A. Holobar, "Characterization of human motor units from surface EMG decomposition," *Proc. IEEE*, vol. 104, no. 2, pp. 353–373, Feb. 2016.

[5] D. Farina and A. Holobar, "Human-Machine interfacing by decoding the surface electromyogram [life sciences]," *IEEE Signal Process. Mag.*, vol. 32, no. 1, pp. 115–120, Jan. 2015.

[6] D. Y. Barsakcioglu and D. Farina, "A real-time surface emg decomposition system for non-invasive human-machine interfaces," in *Proc. IEEE Biomed. Circuits Syst. Conf.*, 2018, pp. 1–4.

[7] D. Y. Barsakcioglu *et al.*, "Control of spinal motoneurons by feedback from a non-invasive real-time interface," *IEEE Trans. Biomed. Eng.*, vol. 68, no. 3, pp. 926–935, Mar. 2021.

[8] V. Glaser, A. Holobar, and D. Zazula, "Real-time motor unit identification from high-density surface EMG," *IEEE Trans. Neural Syst. Rehabil. Eng.*, vol. 21, no. 6, pp. 949–958, Nov. 2013.

[9] E. A. Clancy, E. L. Morin, and R. Merletti, "Sampling, noise-reduction and amplitude estimation issues in surface electromyography," *J. Electromyogr. Kinesiol.*, vol. 12, pp. 1–16, 2002.

[10] E. Huigen, A. Peper, and C. A. Grimbergen, "Investigation into the origin of the noise of surface electrodes," *Med. Biol. Eng. Comput.*, vol. 40, no. 3, pp. 332–338, 2002.

[11] G. Piervirgili, F. Petracca, and R. Merletti, "A new method to assess skin treatments for lowering the impedance and noise of individual gelled agAgCl electrodes," *Physiol. Meas.*, vol. 35, no. 10, pp. 2101–2118, Sep. 2014.

[12] K. Petkos *et al.*, "A high-performance 8 nV/$\sqrt{Hz}$ 8-channel wearable and wireless system for real-time monitoring of bioelectrical signals," *J. NeuroEngineering Rehabil.*, vol. 16, pp. 1–24, 2019.

[13] G. C. Zafeiropoulos and E. M. Drakakis, "The neoEEG board: A. 3 nV/Hz multi-channel wireless instrument for neonatal EEG monitoring," *Measurement: J. Int. Meas. Confederation*, vol. 154, 2020, Art. no. 107442.

[14] E. Mastinu, B. Hakansson, and M. Ortiz-Catalan, "Low-cost, open source bioelectric signal acquisition system," in *Proc. IEEE 14th Int. Conf. Wearable Implantable Body Sensor Netw.*, 2017, pp. 19–22.

[15] G. L. Cerone, A. Botter, and M. Gazzoni, "A modular, smart, and wearable system for high density sEMG detection," *IEEE Trans. Neural Syst. Rehabil. Eng.*, vol. 66, no. 22, pp. 3371–3380, Dec. 2019.

[16] P. Tallgren *et al.*, "Evaluation of commercially available electrodes and gels for recording of slow EEG potentials," *Clin. Neuriophysiol.*, vol. 116, no. 4, pp. 799–806, 2005.

[17] C. J. De Luca *et al.*, "Filtering the surface EMG signal: Movement artifact and baseline noise contamination," *J. Biomech.*, vol. 43, no. 8, pp. 1573–1579, 2010.

[18] L. McManus *et al.*, "Consensus for experimental design in electromyography (CEDE) project: Terminology matrix," *J. Electromyogr. Kinesiol.*, vol. 59, 2021, Art. no. 102565.

[19] A. Holobar, M. A. Minetto, and D. Farina, "Accurate identification of motor unit discharge patterns from high-density surface emg and validation with a novel signal-based performance metric," *J. Neural Eng.*, vol. 11, no. 1, 2014, Art. no. 016008.

[20] R. Merletti and S. Muceli, "Tutorial. surface EMG detection in space and time: Best practices," *J. Electromyogr. Kinesiol.*, vol. 49, 2019, Art. no. 102363.

[21] P. Fortier, "Use of spike triggered averaging of muscle activity to quantify inputs to motoneuron pools," *J. Neuriophysiol.*, vol. 72, no. 1, pp. 248–265, 1994.